Nanoscale



PAPER

View Article Online
View Journal | View Issue



Cite this: Nanoscale, 2020, 12, 23116

Large-area 2D PtTe₂/silicon vertical-junction devices with ultrafast and high-sensitivity photodetection and photovoltaic enhancement by integrating water droplets†

Mashiyat Sumaiya Shawkat, a,b Tanvir Ahmed Chowdhury, Hee-Suk Chung, Shahid Sattar, E Tae-Jun Ko,a J. Andreas Larsson and Yeonwoong Jung ka,b,f

2D PtTe₂ layers, a relatively new class of 2D crystals, have unique band structure and remarkably high electrical conductivity promising for emergent opto-electronics. This intrinsic superiority can be further leveraged toward practical device applications by merging them with mature 3D semiconductors, which has remained largely unexplored. Herein, we explored 2D/3D heterojunction devices by directly growing large-area (>cm²) 2D PtTe₂ layers on Si wafers using a low-temperature CVD method and unveiled their superior opto-electrical characteristics. The devices exhibited excellent Schottky transport characteristics essential for high-performance photovoltaics and photodetection, *i.e.*, well-balanced combination of high photodetectivity (>10¹³ Jones), small photo-responsiveness time (~1 µs), high current rectification ratio (>10⁵), and water super-hydrophobicity driven photovoltaic improvement (>300%). These performances were identified to be superior to those of previously explored 2D/3D or 2D layer-based devices with much smaller junction areas, and their underlying principles were confirmed by DFT calculations.

Received 31st July 2020, Accepted 22nd October 2020 DOI: 10.1039/d0nr05670g

rsc.li/nanoscale

Introduction

Recently, interest in the family of noble metal-based twodimensional (2D) crystals is on the rise owing to their superior electrical properties compared to those of conventional 2D transition metal dichalcogenides (TMDs).^{1–5} Although a large number of semiconducting 2D TMD layers have been explored for unconventional opto-electronics,^{6,7} their carrier mobility values still remain uncompetitive with those of traditional semiconductors.^{8,9} In this regard, noble metal (particularly, platinum (Pt))-based ones provide distinguishable advantages of high carrier mobility^{10–15} and air stability even better than

devices by directly growing metallic 2D PtTe2 layers on pre-pat-

black phosphorus (BP) as well as low-temperature

synthesis. 16,17 2D platinum ditelluride (PtTe₂) layers are a

recent addition to them and exhibit a large set of unparalleled properties compared to other Pt-based 2D TMD layers. 18-20 Most notably, they exhibit an extremely high electrical conductivity of >10⁶ S m⁻¹ - superior to most of the previously reported 2D TMD layers, which is well maintained even with scalable wafer-level growth. 1,21-23 Such intrinsic superiority is projected to be further promoted when they are merged with conventional 3D semiconductors yielding well-controlled 2D/ 3D heterojunctions, particularly for opto-electronic applications.²⁴ In general, such 2D/3D heterojunctions exist in two distinct configurations, i.e., lateral vs. vertical, determined by the ways that 2D layers are interfaced with the 3D materials. Although the lateral integration of small-sized 2D flakes onto 3D semiconductors has accomplished high photosensitivity, the resulting devices exhibited limited photo-response speeds in the range of a few-to milli-seconds.25-27 The vertical integration approach would provide advantages of small diffusion length and depletion dimensions for photo-generated carriers, thereby leading to faster photo-responsiveness. However, it remains difficult to achieve 2D/3D vertical junctions on a laterally large (~cm2) dimension via a scalable process avoiding the unreliable manual transfer of 2D layers. 28,29 Herein, we fabricated large-area (~cm²) PtTe₂/Si 2D/3D vertical heterojunction

^aNanoScience Technology Center, University of Central Florida, Orlando, Florida 32826, USA. E-mail: yeonwoong.jung@ucf.edu

^bDepartment of Electrical and Computer Engineering, University of Central Florida, Orlando, Florida 32816, USA

^cDepartment of Mechanical and Aerospace Engineering, University of Central Florida, Orlando, Florida 32816, USA

^dAnalytical Research Division, Korea Basic Science Institute, Jeonju 54907, South Korea

^eApplied Physics, Division of Materials Science, Department of Engineering Sciences and Mathematics, Luleå University of Technology, Luleå SE 97187, Sweden

^fDepartment of Materials Science and Engineering, University of Central Florida, Orlando, Florida 32816. USA

 $[\]dagger$ Electronic supplementary information (ESI) available. See DOI: 10.1039/d0nr05670g

Nanoscale Paper

terned Si wafers using a scalable chemical vapor deposition (CVD) method. We unveiled their "intrinsically" superior photovoltaic and photodetection performances over previously explored devices as well as identifying methods to "externally" further promote such superiority.

Experimental

Device fabrication

300 nm SiO₂ was deposited on a cleaned Si wafer through a shadow mask at a rate of 1 Å s⁻¹ by electron-beam evaporation (Thermionics VE-100). A Pt film was deposited on the prepared SiO₂/Si wafer through another shadow mask at a rate of 0.05 Å s⁻¹, defining Pt/Si active and Pt/SiO₂ electrode areas. The prepared sample was transferred to the middle of a quartz tube CVD furnace, and Te powders were placed in an alumina boat at the furnace upstream side. The tube was purged with argon (Ar) gas and pumped to a base pressure of ~1 mTorr. The furnace temperature was ramped up to 400 °C in 50 min and then maintained at the temperature for another 50 min. Throughout the reaction, Ar gas was constantly flowed (100 SCCM) through the tube, maintaining its operating pressure at ~80 mTorr. Once the PtSe₂/SiO₂/Si samples were prepared, Au electrodes (50 nm thickness) were deposited through another shadow mask using a Quorum Q150 T Plus sputtering system.

TEM and Raman characterization

Microstructure analysis of 2D PtTe₂ layers was performed with a JEOL ARM 200 F Cs-corrected TEM at an operating voltage of 200 kV. For the plane-view TEM characterization of 2D PtTe₂ layers, we directly grew them on a SiO₂/Si wafer and applied a buffered oxide etchant (BOE) to the as-grown 2D PtTe₂ layer-SiO₂/Si sample. The BOE gently etched away the underlying SiO₂, lifting off the 2D PtTe₂ layers only. The delaminated 2D PtTe₂ layers were transferred onto copper TEM grids. For the cross-sectional TEM sample preparation, focused ion beam (FIB; Quanta 2D FEG, FEI)-based milling and lift-out techniques were employed. For Raman spectroscopy characterization, a Renishaw RM 1000B system with a laser source of 514 nm wavelength was used.

Electrical and photovoltaic characterization

All electrical measurements were performed with a home-built probe station using a HP 4156 A semiconductor parameter analyzer. Photovoltaic measurements were carried out using an AM 1.5 solar simulator (G2V optics). Photo-response measurements were carried out using a M625L4-C2 (625 nm) Thorlabs LED. The response speed was characterized using a home-built measurement system using a Tektronix MDO4104C digital oscilloscope. The frequency modulation of the LED source was carried out using a Tektronix AFG 3022C function generator.

Water contact angle measurements

Water contact angles of 2D PtTe₂ layers were measured with a goniometer (model 90, Ramé-Hart Instrument Co.). Water droplets (2 μ L) were gently integrated on the surface of as-grown 2D PtTe₂ layers using a micro-syringe, and the contact angle values were extracted using the DROPimage Pro software (Ramé-Hart Instrument Co.).

Results

Fig. 1 shows the preparation of PtTe₂/Si devices and the structural/chemical characterization of the adopted 2D PtTe₂ layers. Fig. 1a illustrates the sequential procedures for the device fabrication, starting with the patterned deposition of silicon dioxide (SiO₂) on p-doped Si wafers (resistivity \sim 1–5 Ω cm). Pt thin films of controlled thickness are selectively deposited on the wafers via an electron beam evaporator using a shadow mask. Subsequently, 2D PtTe2 layers are grown at 400 °C through the CVD tellurization method developed in our previous studies, 1,23 defining the lateral dimension of PtTe₂/Si vertical heterojunctions. Lastly, gold (Au) electrodes are selectively deposited on the top PtTe2/SiO2 side as well as the wafer bottom side. Details of the sample preparation are presented in the Experimental section. Fig. 1b shows the representative image of a complete PtTe2/Si device with Au electrodes. Fig. 1c shows the Raman spectroscopy characterization of few-layered 2D PtTe₂ obtained by the CVD tellurization of Pt ~0.3 nm, comparing experimentally determined (blue dotted line) vs. theoretically calculated (black solid line) characteristics. Two characteristic peaks of E_g and A_{1g} are noted, where E_g (A_{1g}) peaks depict the in-plane (out-of-plane) vibrational modes of Te atoms within the 2D layers, respectively. Excellent agreement is observed between these two spectra of experimental vs. theoretical in terms of their peak positions. The atomic crystallinity of the CVD-grown 2D PtTe2 layers was studied using a scanning transmission electron microscope (STEM). Fig. 1d presents the dark-field STEM image of the as-grown 2D PtTe₂ layers, unveiling a large number of polycrystalline grains. Each grain is individually "stitched" with respect to its neighbouring ones, achieving a high spatial homogeneity over the entire sample area. The inset in Fig. 1d is the corresponding selective area diffraction (SAED) pattern, showing the dominant appearance of the (110) PtTe₂ plane. Fig. 1e shows the plane-view high-resolution (HR) STEM image of the polycrystalline 2D PtTe2 layers, revealing two adjacent stitching grains separated by the grain boundary (purple curve). Each grain exhibits distinguishable Moiré fringes, indicating vertical stacking of individual 2D layers with misaligned crystallographic orientation. Fig. 1f shows the cross-sectional HRSTEM image to reveal the well-defined van der Waals (vdW) gaps in vertically stacked 2D PtTe2 layers, indicating their layer-by-layer growth. Fig. 1g shows the corresponding energy-dispersive X-ray spectroscopy (EDS) elemental mapping images, unveiling the spatial homogeneity of constituent elements.

Paper Nanoscale

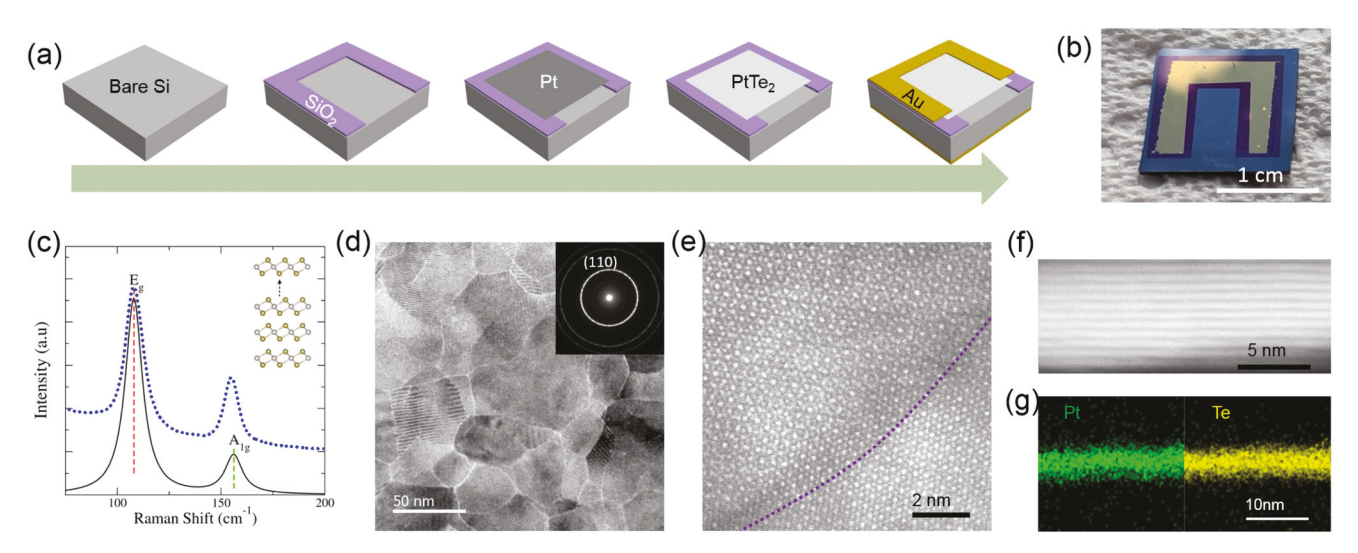


Fig. 1 (a) Schematic illustration of sequential steps for fabricating PtTe₂/Si heterojunction devices. (b) Image of a complete PtTe₂/p-Si Schottky junction device. (c) Raman spectroscopy characterization of few-layered 2D PtTe₂, comparing the theoretically calculated spectrum (black solid line) with the experimentally determined one (blue dotted line). (d) Plane-view STEM image of 2D PtTe₂ layers and the corresponding SAED pattern in the inset. (e) Plane-view HR-STEM image revealing two neighboring stitching grains, separated by the grain boundary (purple dotted curve). (f) Cross-sectional HR-STEM image of 2D PtTe₂ multilayers. (g) Cross-sectional STEM-EDS elemental mapping images corresponding to (f).

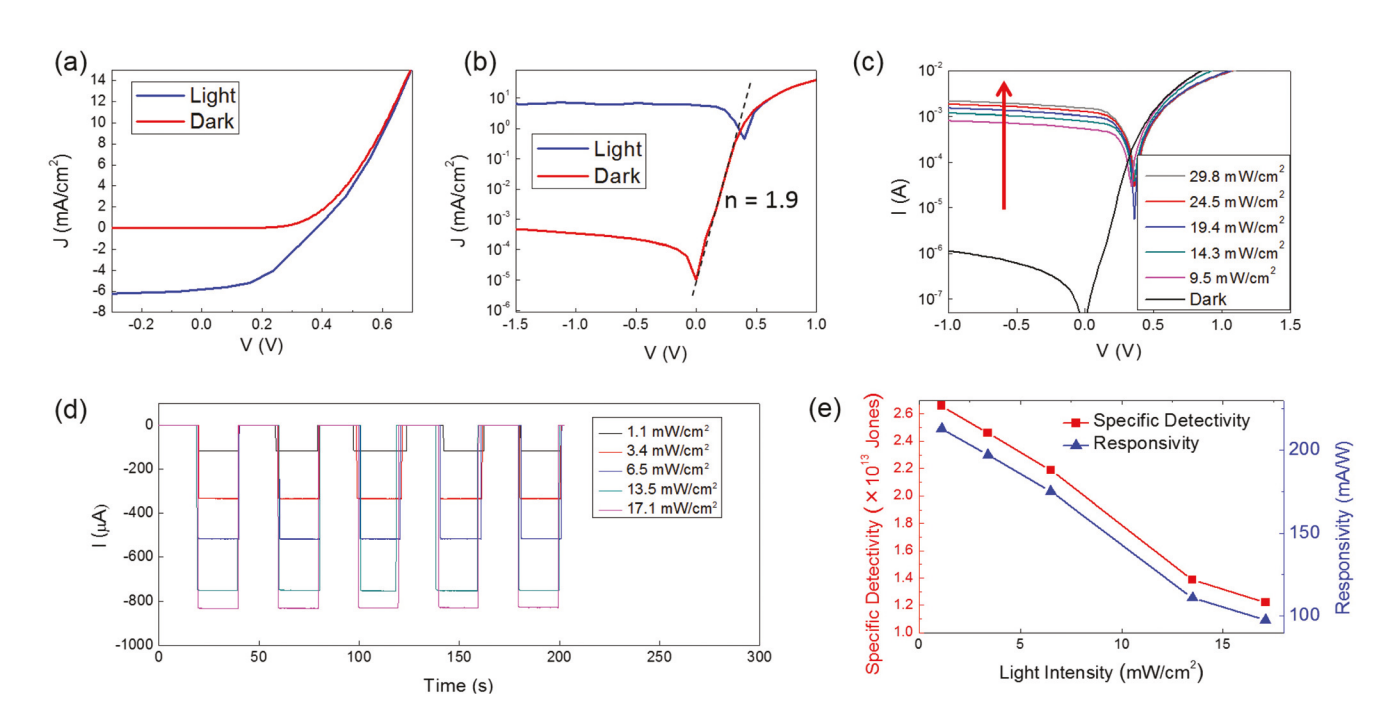


Fig. 2 (a–c) Photovoltaics of $PtTe_2/p-Si$ devices prepared with Pt of 4.5 nm thickness; (a) J-V characteristics in the dark (red) and under illumination (blue), and (b) the corresponding presentation in the semi-log scale. (c) I-V characteristics of another device in the semi-log scale measured under 625 nm illumination of varying intensities. (d and e) Photo-responsiveness measured at zero external bias; (d) Temporal response of a device under 625 nm illumination of varying intensities. (e) Light intensity-dependent specific detectivity (red) and responsivity (blue) of the same device in (d).

Fig. 2 shows the electrical properties of the stand-alone 2D PtTe₂ layers as well as the PtTe₂/Si heterojunction devices. The CVD-2D PtTe₂ layers exhibit an extremely high electrical conductivity of $\sim 10^5 - 10^6$ S m⁻¹ and intrinsically metallic transport characteristics irrespective of their layer numbers, as con-

firmed in our previous studies.¹ For further clarification, we characterized their transport properties in field effect transistor (FET) configurations, and confirmed no noticeable gate responses (Fig. S1, ESI†). Additionally, we identified their electronic band structure by density functional theory (DFT) calcu-

Nanoscale Paper

lations³⁰ and confirmed strong metallic dispersion characteristics (Fig. S2, ESI†). Having confirmed the highly metallic nature of 2D PtTe2 layers, we developed the heterojunction devices by optimizing their layer thickness. Fig. 2a shows the photovoltaic characterization of the device incorporating 2D PtTe₂ layers prepared with Pt of an ~4.5 nm thickness, revealing the current density-voltage (J-V) characteristics without (red) and with (blue) a solar illumination (intensity: 400 W m⁻²). The device shows pronounced photovoltaic effects corroborated by a large amount of photo-induced current density in the reverse bias regime. Fig. 2b presents the corresponding J-V plot in a semi-log scale, yielding the following parameters; open circuit voltage $(V_{\rm oc}) \sim 0.41$ V, short circuit current density $(J_{\rm sc})$ ~5.9 mA cm⁻², fill factor (FF) ~44%, and rectification ratio $\sim 10^5$ at ± 1.5 V. The device ideality factor, n, extracted from the linearity (black line) in the forward bias regime is \sim 1.9 and the power conversion efficiency (PCE) is \sim 2.5%. This observation of strong current rectification and photovoltaic characteristics confirms the presence of metal (PtTe₂)-semiconductor (Si) Schottky junctions whose mechanism will be discussed in the next section. Additionally, we confirmed the Ohmic transport characteristics from 2D PtTe2 layers and p-Si wafers interfaced with Au electrodes (Fig. S3, ESI†), which further confirms that the rectification originates from the junctions. Representative data obtained from the devices prepared with smaller (~0.3 nm) and larger (~13.5 nm) Pt thickness are presented in Fig. S4, ESI†, confirming inferior performances compared to the optimized one. This thickness-sensitive photovoltaic performance is attributed to the competing effect of thickness-dependent optical transmittance vs. electrical conductivity as confirmed in our previous studies. 1,23 The optical transmittance steeply decreases with increasing thickness, while the electrical properties are less thickness-sensitive exhibiting maximum conductivity at a certain thickness due to the anisotropic crystallinity of 2D PtTe₂ layers. 1,23 We note that these PtTe₂/Si heterojunction devices perform much better than the previously explored Pt TMD-based ones including platinum diselenide (PtSe₂)/Si of comparable thickness, ¹² i.e., an increase of \sim 15% and \sim 47% for $V_{\rm oc}$ and $J_{\rm sc}$, respectively. In addition to photovoltaics, we also investigated their photoresponsiveness using an illumination source of a fixed wavelength. Fig. 2c shows the semi log-scaled I-V characteristics of another device different from the one in Fig. 2a and b under intensity-varying illumination at 625 nm wavelength. The photocurrent at the reverse bias regime steadily increases with increasing intensity, reflecting the increasing concentration of photo-generated charge carriers.31 Fig. 2d shows the timedependent train of photocurrent generation at a zero external bias under periodic illumination of varying intensities revealing highly reliable photo-responsiveness. We also confirmed that the device was still very sensitive even at a much lower intensity of 0.1 mW cm⁻² (Fig. S5, ESI†). Photo-responsivity and specific detectivity are two key parameters used to evaluate the photo-responsiveness performance of the device; photoresponsivity, R, indicates its efficiency in responding to changes in optical signals, whereas specific detectivity, D^* ,

delineates its ability to detect small signals. They are obtained from the following equations. ^{32,33}

$$R = \frac{I_{\rm ph}}{P_{\rm in}} \tag{1}$$

$$D^* = \frac{A^{\frac{1}{2}}R}{(2eI_{\mathbf{d}})^{\frac{1}{2}}} \tag{2}$$

where $I_{\rm ph}$, $I_{\rm d}$, $P_{\rm in}$, A and e are the photocurrent, dark current, incident light power, active device area, and elementary charge, respectively. Fig. 2e presents the plots of R (blue) and D^* (red) vs. light intensity extracted from the above equations for the PtTe2/Si device at a zero external bias. Both R and D* show the inverse relationship with intensity, consistent with the observations with other 2D/3D photodetectors. 31,34,35 The R value reaches up to 0.213 A W⁻¹ at an intensity of 1.1 mW cm⁻², comparable to those of other 2D/3D photodetectors at a zero external bias. 32,35,36 Furthermore, the D* value is as high as 2.66×10^{13} Jones, which is much higher than those of previously developed 2D/3D and stand-alone 2D devices - to be confirmed in the next section. This finding is particularly encouraging given that the lateral dimension of the active junction area in our device is quite large (1 cm × 0.5 cm), while previous developments mostly employed small-sized (typically, $\sim \mu m^2$) exfoliated 2D flakes. Additionally, the external quantum efficiency (EQE) of the device was extracted using the following equation:

$$EQE = \frac{hcR}{e\lambda}$$
 (3)

which yields a moderately high ECE of 42.2%. In the above equation, h is Planck's constant, c is the velocity of light, R is the responsivity, and λ is the wavelength of the illumination source. Key parameters of various 2D/3D photodetectors operated at a zero bias are compared and presented in Table 1, ESI.† It is noted that the perfomance of our PtTe₂/Si device is comparable to those of the previously explored ones despite its much larger junction area.

Furthermore, we studied the practical suitability of the PtTe₂/Si device for high-performance photodetection applications. Particularly, photo-response speed is of paramount importance in optical communication and imaging applications as it dictates their efficiency for optical-to-electrical signal conversion. For the precise quantification of response speed, a 625 nm wavelength light was pulsed and introduced to the device using a signal generator as demonstrated in Fig. 3a. The temporal photo-response of the device at a zero external bias was recorded using a digital oscilloscope at several frequencies. Fig. 3b-d present the normalised transient photocurrents generated by the pulsed illumination with frequencies of 10 Hz, 30 kHz and 300 kHz, respectively. The results show well-resolved and retained photo-responsiveness even up to a very high frequency of 300 kHz for multiple cycles, confirming fast and reliable photo-switching. Fig. 3e presents the relative current balance of the device, i.e., $(I_{\text{max}} I_{\min}$)/ I_{\max} , as a function of modulation frequency, where I_{\max}

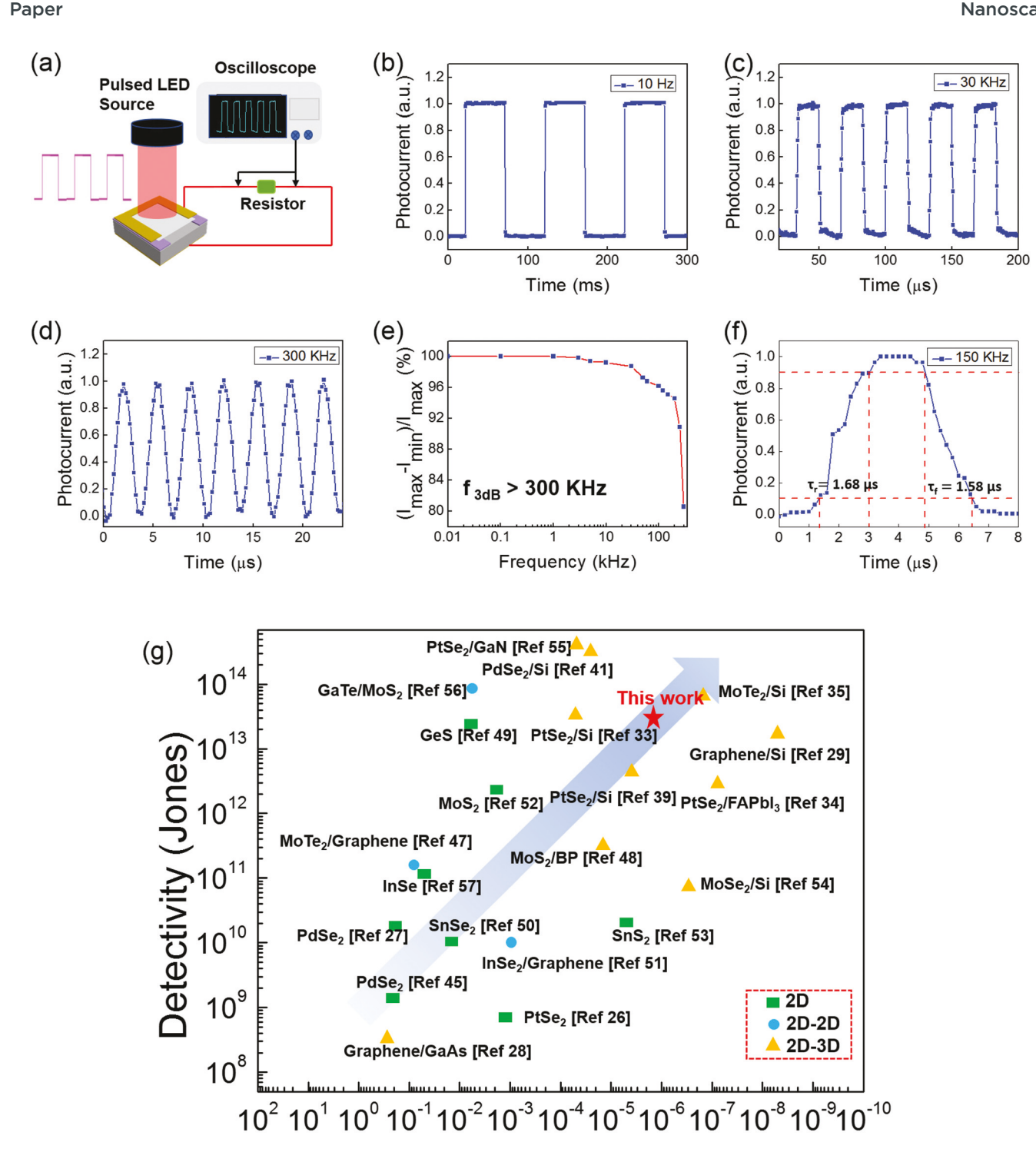


Fig. 3 (a) Schematic illustration of the experimental setup for recording the temporal photo-responsiveness of PtTe₂/p-Si devices under periodically pulsed 625 nm illumination. (b-d) Temporal photo-responsiveness of a device measured at varying illumination frequencies of (b) 10 Hz, (c) 30 kHz, and (d) 300 kHz. (e) Relative balance, $(I_{\text{max}} - I_{\text{min}})/I_{\text{max}}$, of the same device as a function of illumination modulation frequency revealing a 3-dB cutoff frequency of >300 kHz. (f) Magnified view of photo-switching characteristics obtained at 150 kHz clarifying rise (τ_r) and fall (τ_f) times. (g) Comparison of photo-responsiveness performances between the PtTe₂/p-Si device in this work vs. other 2D, 2D-2D, and 2D-3D heterojunction devices in previous reports.

Response Time (s)

Nanoscale

 (I_{\min}) is the maximum (minimum) current obtained at each frequency with (without) illumination over multiple cycles, respectively. A high balance of >95% is well preserved up to a frequency of 100 kHz, after which it steadily attenuates with increasing frequencies. This current attenuation still maintains ~80.6% of its maximum value even at a very high frequency of 300 kHz, significantly surpassing the 3-db cut-off frequency standard in commercial applications^{37,38} as well as the values observed with previously developed 2D/3D devices. 32,33,39 Fig. 3f shows the representative plot of the photocurrent generation/decay transient characteristics obtained at 150 kHz, quantifying photoresponse intervals. The rise (τ_r) and fall (τ_f) times are determined from the 90% and 10% of the maximum current value, respectively, yielding $\tau_r \sim$ 1.68 μ s and $\tau_f \sim 1.58 \mu$ s, respectively. Comparison is made between the PtTe2/Si device vs. previously developed 2D layerbased devices in terms of photo-detectivity and response time, as shown Fig. 3g. What is noteworthy is that this PtTe2/Si device exhibits well-balanced characteristics of high photodetectivity and fast photo-responsiveness, while responsitivity, R, is observed to be similar in the measured wavelength range $(\sim 600-850 \text{ nm})$, $^{32-34,36,38-43}$ both the response time and photodetectivity are much better than those observed with most of 2D/3D, 2D/2D, and stand-alone 2D layer-based devices. 27,28,33,34,39,41,44-55 This is particularly encouraging given the large (~0.5 cm²) lateral dimension of the PtTe₂/Si junction enabled by the scalable CVD growth, while a large number of the previously developed ones are based on the manual integration of small-sized 2D flakes. 26-29,41,45,47,54,56,57 For instance, although the graphene/Si device²⁹ shown in Fig. 3g exhibits slightly faster photo-response, its active junction area is only ~0.25 mm² which is 200 times smaller than that of ours. Furthermore, the MoTe₂/Si device³⁵ shown in Fig. 3g slightly outperforming our device demanded a manual integration of additional graphene top layers, thus limiting its process scalability. 43 Meanwhile, our PtTe2/Si devices exhibit "intrinsic" 2D/3D Schottky junction characteristics un-aided by any additional materials and processes preserving a low-temperature growth scalability.

To confirm the charge transport mechanism of the device, we study the PtTe₂/Si heterojunction contact characteristics by theoretically determining its Schottky barrier height using first principles calculations. The planar average electrostatic potential (PAEP) of the PtTe2/Si interface is computed in the out-ofplane direction along the Si (100) orientation, as presented in Fig. 4a. The work function of few-layered 2D PtTe₂, $\Phi_{\rm M}$, is defined as $\Phi_{\rm M}$ = $E_{\rm vac}$ – $E_{\rm Fermi}$, where $E_{\rm vac}$ is the vacuum level set to 0 eV to calibrate the energy scale, and E_{Fermi} is the highest occupied electron energy state at 0 K.58 The work function value is determined to be ~4.56-4.57 eV with the layer number ranging from three to six. We also computed the band offset and the work function of p-Si by superimposing the PAEP of bulk Si on that of the slab (Fig. S6, ESI†). The PAEP diagram in Fig. 4b shows the work function of p-Si, Φ_{Si} , is ~4.95 eV, determined from the experimental bandgap (~1.1 eV) of Si. Since the work function of the metallic 2D PtTe₂

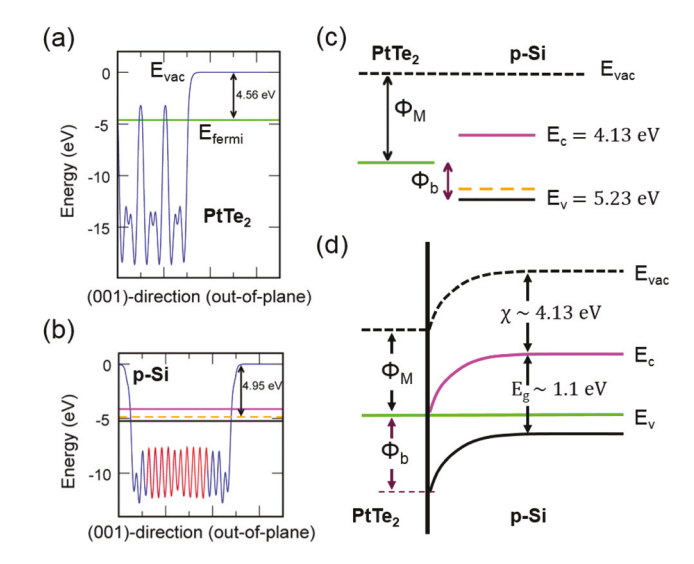


Fig. 4 (a) PAEP diagram of few layered 2D PtTe₂ and its calculated work function, (4.56 eV, green line) with the vacuum level at 0 eV. (b) Determination of the work function of p-Si (4.95 eV, orange line) and band offsets by superimposing the PAEP of bulk Si on that of the slab and calibrating the vacuum level to 0 eV. (c) Energy band diagrams for 2D PtTe₂ and p-Si that form a p-type Schottky contact upon interfacing. (d) Band bending diagram revealing the presence of PtTe₂/p-Si Schottky barrier whose height is determined to be 0.67 eV (violet line).

layers is smaller than that of p-Si, a p-type Schottky junction is anticipated to form when these two materials are interfaced, as depicted in Fig. 4c. To determine the Schottky barrier height, $\Phi_{\rm b}$, for this junction, we refer to the known equation, $\Phi_{\rm b} = E_{\rm g} + \chi - \Phi_{\rm M}$, where $E_{\rm g}$ (~1.1 eV) is the bandgap and χ (~4.13 eV) is the electron affinity of Si, and $\Phi_{\rm M}$ is the work function of 2D PtTe2 layers. We identify that 2D PtTe2 layers form an obvious Schottky junction, yielding $\Phi_b = 0.67$ eV. Fig. 4d shows the diagram of the energy band bending at the PtTe₂/p-Si interface, which strongly justifies that the experimentally observed characteristics are a result of 2D/3D Schottky junctions. In the diagram, E_c , and E_V represent the conduction and valence band edge of Si, respectively. The details of the computational method are presented in the Computational section (ESI†). We also determined the Φ_b value by analysing experimentally obtained I-V characteristics and observed good agreement with the theoretically calculated one (Fig. S7, ESI†).

Lastly, we demonstrated externally tunable opto-electrical properties in the PtTe₂/Si devices by taking advantage of the intrinsic structural uniqueness of 2D PtTe₂ layers. We identified that the large-area 2D PtTe₂ layers intrinsically exhibit "super-hydrophobic" surfaces as manifested by the very large (>110°) water contact angle as shown in Fig. 5a. Indeed, this hydrophobicity is the highest among all previously explored 2D TMD layers, ^{60,61} which can be exploited to further improve device performances as presented in Fig. 5b–g. Fig. 5b shows the representative *I–V* characteristics of an identical PtTe₂/Si device under three different conditions; *i.e.*, in the dark (blue), under illumination (red), and under the same illumination

Paper Nanoscale

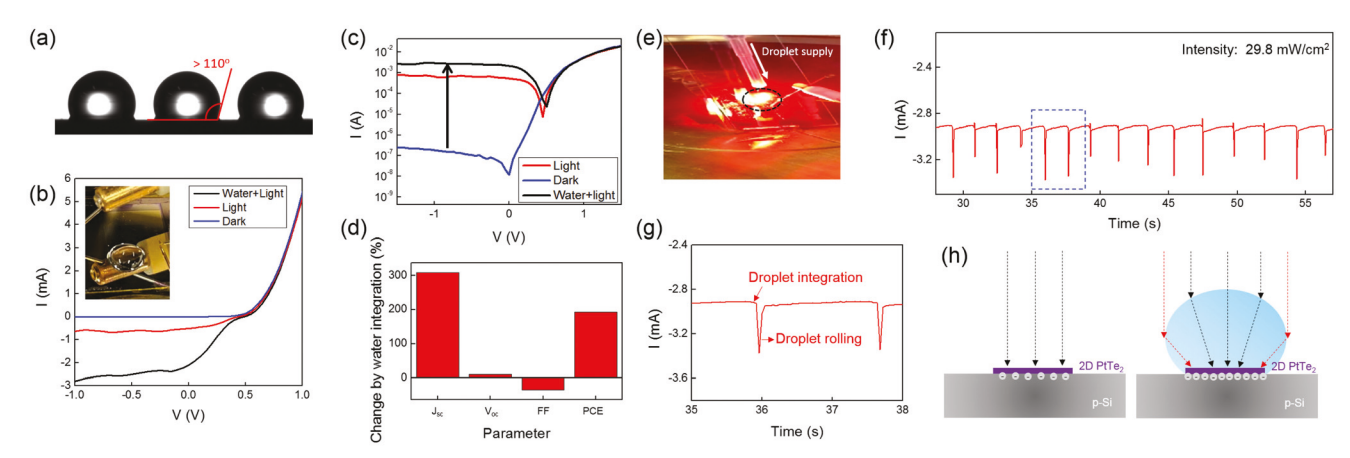


Fig. 5 (a) Image of water droplets integrated on a PtTe₂/p-Si device. (b) I-V characteristics of the PtTe₂/p-Si device in the dark (blue), under illumination (red), and after integrating the water droplet shown in the inset (black). (c) I-V characteristics in the semi-log scale corresponding to (b). (d) Change of photovoltaic parameters induced by the water droplet integration in (b) and (c). (e) Integration of water droplets on the PtTe2/p-Si device slanted at ~45° under continuous illumination from a 625 nm LED source at an intensity of 29.8 mW cm⁻². (f) Temporal current obtained from the device in (e) with a periodic integration of water droplets at an interval of ~1.6 s. (g) Enlarged view of the blue dotted region in (f) highlighting the current change by the droplet integration and rolling-off due to gravity. (h) Schematic illustration of the increased concentration of photo-generated carriers by the light concentration effect.

with water droplet integration (black) which drastically improved the photovoltaic effect as manifested by a significant increase in reverse current. Fig. 5c shows the corresponding semi-log scaled I-V characteristics, better visualizing the photovoltaic enhancement. Fig. 5d shows the summary of the water droplet-driven change in photovoltaic parameters, revealing enhancements in $J_{\rm sc}$ by ~309%, $V_{\rm oc}$ by ~9%, PCE by ~192%, and a reduction of FF by ~35%. The much larger enhancement in J_{sc} over the other parameters indicates the significantly increased concentration of photo-generated charge carriers. Photo-responsiveness of another device slanted at ~45° was also evaluated under a continuous illumination (29.8 mW cm⁻² intensity and 625 nm wavelength) by periodically integrating water droplets on it, as shown in Fig. 5e. Fig. 5f presents the corresponding temporal photo-responsiveness, revealing that a train of current spikes periodically appears following the periodic water droplet application. Fig. 5g corresponds to the blue box in Fig. 5f, highlighting the periodic and instant increase in reverse current upon integrating water droplets, measured at a voltage of -2 V. The current reversibly returns to the original value once the droplets subsequently roll down from the sample surface and disappear. We believe that this significant increase in reverse current is the result of the light concentration effect introduced by the integrated water droplets; i.e. the hemispherical water droplet caused by the super-hydrophobic surface enables the in-ward refraction of incident light rays increasing the concentration of photo-generated charge carriers, as schematically illustrated in Fig. 5h. The phenomenon is qualitatively consistent with the effects resulting from integrating light concentrating optical lenses on top of photovoltaic cells.⁶² Indeed, Li et al. demonstrated significantly enhanced photovoltaic effects by directly integrating water droplets onto the surface of hydrophobic carbon-nanotube photovoltaic cells,63 which well agrees with

the observation in this study. As a control experiment to verify this hypothesis, we prepared a glass slide with hydrophobic coating and integrated it on top of the PtTe2/Si device. We then integrated water droplets on top of the glass slide/device and performed photovoltaic measurements, mimicking the experiments in Fig. 5f and g. As predicted, a significant increase in photocurrent is observed by integrating water droplets (Fig. S8, ESI†), which decisively confirms the super-hydrophobicity enabled light concentration effect.

Conclusions

In summary, we have developed the large-area PtTe₂/Si heterojunction devices by directly growing metallic 2D PtTe2 multilayers on p-Si wafers and explored their photovoltaic and photodetection properties. The devices exhibit a comprehensive set of promising Schottky junction characteristics, i.e., large rectification ratio, small ideality factor, high photosensitivity and small photoresponse time. Extensive comparisons with previously explored 2D layer-based similar devices confirm their excellence in high-efficiency opto-electrical applications. Furthermore, the devices present improved performances upon integrating water droplets on their surfaces owing to the unusually high hydrophobic nature of 2D PtTe2 layers. This study is believed to greatly broaden the versatility of 2D PtTe2 layers - a relatively unexplored 2D crystal with high electrical conductivity - towards scalable 2D/3D hybrid device applications in a wide range of emerging opto-electronics.

Conflicts of interest

There are no conflicts to declare.

Nanoscale Paper

Acknowledgements

Y. J. acknowledges financal supports from the National Science Foundation (CMMI-1728390) (M. S. S., and Y. J.), the Korea Institute of Energy Technology Evaluation and Planning (KETEP) and the Ministry of Trade, Industry & Energy (MOTIE) of the Republic of Korea (no. 20173010013340), and the VPR Advancement of Early Career Researchers award from the University of Central Florida. S. S. and J. A. L. thank the Knut och Alice Wallenberg Foundation, Kempestiftelserna and Interreg Nord for financial support. S. S. and J. A. L. also thank the High Performance Computing Center North (HPC2N), the National Supercomputer Center in Linköping (NSC), and the PDC Center for High Performance Computing for allocation of time and resources, through the Swedish National Infrastructure for Computing (SNIC). The authors thank Drs. Putnam and Roy for experimental support in his interfacial transport laboratory and in her next-generation electronics laboratory, respectively.

Notes and references

- 1 M. Wang, T.-J. Ko, M. S. Shawkat, S. S. Han, E. Okogbue, H.-S. Chung, T.-S. Bae, S. Sattar, J. Gil, C. Noh, K. H. Oh, Y. Jung, J. A. Larsson and Y. Jung, ACS Appl. Mater. Interfaces, 2020, 12, 10839–10851.
- S. S. Han, J. H. Kim, C. Noh, J. H. Kim, E. Ji, J. Kwon,
 S. M. Yu, T.-J. Ko, E. Okogbue, K. H. Oh, H.-S. Chung,
 Y. Jung, G.-H. Lee and Y. Jung, ACS Appl. Mater. Interfaces,
 2019, 11, 13598–13607.
- 3 E. Okogbue, S. S. Han, T.-J. Ko, H.-S. Chung, J. Ma, M. S. Shawkat, J. H. Kim, J. H. Kim, E. Ji, K. H. Oh, L. Zhai, G.-H. Lee and Y. Jung, *Nano Lett.*, 2019, 19, 7598–7607.
- 4 Y. Jung, J. Shen, Y. Liu, J. M. Woods, Y. Sun and J. J. Cha, *Nano Lett.*, 2014, **14**, 6842–6849.
- 5 J. H. Kim, T.-J. Ko, E. Okogbue, S. S. Han, M. S. Shawkat, M. G. Kaium, K. H. Oh, H.-S. Chung and Y. Jung, *Sci. Rep.*, 2019, 9, 1641.
- 6 L. Britnell, R. M. Ribeiro, A. Eckmann, R. Jalil, B. D. Belle, A. Mishchenko, Y. J. Kim, R. V. Gorbachev, T. Georgiou, S. V. Morozov, A. N. Grigorenko, A. K. Geim, C. Casiraghi, A. H. C. Neto and K. S. Novoselov, *Science*, 2013, 340, 1311.
- 7 T.-J. Ko, S. S. Han, E. Okogbue, M. S. Shawkat, M. Wang, J. Ma, T.-S. Bae, S. B. Hafiz, D.-K. Ko, H.-S. Chung, K. H. Oh and Y. Jung, *Appl. Mater. Today*, 2020, 20, 100718.
- 8 G. Fiori, F. Bonaccorso, G. Iannaccone, T. Palacios, D. Neumaier, A. Seabaugh, S. K. Banerjee and L. Colombo, *Nat. Nanotechnol.*, 2014, 9, 768–779.
- 9 D. Akinwande, N. Petrone and J. Hone, *Nat. Commun.*, 2014, 5, 5678.
- 10 A. Ciarrocchi, A. Avsar, D. Ovchinnikov and A. Kis, *Nat. Commun.*, 2018, **9**, 919.
- 11 R. A. B. Villaos, C. P. Crisostomo, Z.-Q. Huang, S.-M. Huang, A. A. B. Padama, M. A. Albao, H. Lin and F.-C. Chuang, *npj 2D Mater. Appl.*, 2019, 3, 2.

- 12 M. S. Shawkat, H.-S. Chung, D. Dev, S. Das, T. Roy and Y. Jung, *ACS Appl. Mater. Interfaces*, 2019, **11**, 27251–27258.
- 13 M. S. Shawkat, J. Gil, S. S. Han, T.-J. Ko, M. Wang, D. Dev, J. Kwon, G.-H. Lee, K. H. Oh, H.-S. Chung, T. Roy, Y. Jung and Y. Jung, ACS Appl. Mater. Interfaces, 2020, 12, 14341– 14351.
- 14 W. Zhang, Z. Huang, W. Zhang and Y. Li, *Nano Res.*, 2014, 7, 1731–1737.
- 15 J. Qiao, X. Kong, Z.-X. Hu, F. Yang and W. Ji, *Nat. Commun.*, 2014, 5, 4475.
- 16 Y. Zhao, J. Qiao, Z. Yu, P. Yu, K. Xu, S. P. Lau, W. Zhou, Z. Liu, X. Wang, W. Ji and Y. Chai, Adv. Mater., 2017, 29, 1604230.
- 17 Y. Wang, L. Li, W. Yao, S. Song, J. T. Sun, J. Pan, X. Ren, C. Li, E. Okunishi, Y.-Q. Wang, E. Wang, Y. Shao, Y. Y. Zhang, H.-T. Yang, E. F. Schwier, H. Iwasawa, K. Shimada, M. Taniguchi, Z. Cheng, S. Zhou, S. Du, S. J. Pennycook, S. T. Pantelides and H.-J. Gao, *Nano Lett.*, 2015, 15, 4013–4018.
- 18 K. Deng, M. Yan, C.-P. Yu, J. Li, X. Zhou, K. Zhang, Y. Zhao, K. Miyamoto, T. Okuda, W. Duan, Y. Wu, X. Zhong and S. Zhou, *Sci. Bull.*, 2019, **64**, 1044–1048.
- 19 M. S. Bahramy, O. J. Clark, B. J. Yang, J. Feng, L. Bawden, J. M. Riley, I. Marković, F. Mazzola, V. Sunko, D. Biswas, S. P. Cooil, M. Jorge, J. W. Wells, M. Leandersson, T. Balasubramanian, J. Fujii, I. Vobornik, J. E. Rault, T. K. Kim, M. Hoesch, K. Okawa, M. Asakawa, T. Sasagawa, T. Eknapakul, W. Meevasana and P. D. C. King, *Nat. Mater.*, 2018, 17, 21–28.
- 20 M. Yan, H. Huang, K. Zhang, E. Wang, W. Yao, K. Deng, G. Wan, H. Zhang, M. Arita, H. Yang, Z. Sun, H. Yao, Y. Wu, S. Fan, W. Duan and S. Zhou, *Nat. Commun.*, 2017, 8, 257.
- 21 L. Fu, D. Hu, R. G. Mendes, M. H. Rümmeli, Q. Dai, B. Wu, L. Fu and Y. Liu, ACS Nano, 2018, 12, 9405–9411.
- 22 H. Ma, P. Chen, B. Li, J. Li, R. Ai, Z. Zhang, G. Sun, K. Yao, Z. Lin, B. Zhao, R. Wu, X. Tang, X. Duan and X. Duan, *Nano Lett.*, 2018, 18, 3523–3529.
- 23 E. Okogbue, T.-J. Ko, S. S. Han, M. S. Shawkat, M. Wang, H.-S. Chung, K. H. Oh and Y. Jung, *Nanoscale*, 2020, 12, 10647–10655.
- 24 L. Wang, J. Jie, Z. Shao, Q. Zhang, X. Zhang, Y. Wang, Z. Sun and S.-T. Lee, *Adv. Funct. Mater.*, 2015, 25, 2910– 2919.
- 25 H. Huang, J. Wang, W. Hu, L. Liao, P. Wang, X. Wang, F. Gong, Y. Chen, G. Wu, W. Luo, H. Shen, T. Lin, J. Sun, X. Meng, X. Chen and J. Chu, *Nanotechnology*, 2016, 27, 445201.
- 26 X. Yu, P. Yu, D. Wu, B. Singh, Q. Zeng, H. Lin, W. Zhou, J. Lin, K. Suenaga, Z. Liu and Q. J. Wang, *Nat. Commun.*, 2018, 9, 1545.
- 27 C. H. Mak, S. Lin, L. Rogée and S. P. Lau, *J. Phys. D: Appl. Phys.*, 2019, **53**, 065102.
- 28 H. Tian, A. Hu, Q. Liu, X. He and X. Guo, *Adv. Opt. Mater.*, 2020, **8**, 1901741.

Paper Nanoscale

- 29 X. Wan, Y. Xu, H. Guo, K. Shehzad, A. Ali, Y. Liu, J. Yang, D. Dai, C.-T. Lin, L. Liu, H.-C. Cheng, F. Wang, X. Wang, H. Lu, W. Hu, X. Pi, Y. Dan, J. Luo, T. Hasan, X. Duan, X. Li, J. Xu, D. Yang, T. Ren and B. Yu, npj 2D Mater. Appl., 2017, 1, 4.
- 30 K. Koumpouras and J. A. Larsson, J. Phys.: Condens. Matter, 2020, 32, 315502.
- 31 L. Zeng, S. Lin, Z. Lou, H. Yuan, H. Long, Y. Li, W. Lu, S. P. Lau, D. Wu and Y. H. Tsang, NPG Asia Mater., 2018, 10, 352-362.
- 32 L.-H. Zeng, Q.-M. Chen, Z.-X. Zhang, D. Wu, H. Yuan, Y.-Y. Li, W. Qarony, S. P. Lau, L.-B. Luo and Y. H. Tsang, Adv. Sci., 2019, 6, 1901134.
- 33 C. Xie, L. Zeng, Z. Zhang, Y.-H. Tsang, L. Luo and J.-H. Lee, Nanoscale, 2018, 10, 15285-15293.
- 34 Z.-X. Zhang, Z. Long-Hui, X.-W. Tong, Y. Gao, C. Xie, Y. H. Tsang, L.-B. Luo and Y.-C. Wu, J. Phys. Chem. Lett., 2018, 9, 1185-1194.
- 35 Z. Lu, Y. Xu, Y. Yu, K. Xu, J. Mao, G. Xu, Y. Ma, D. Wu and J. Jie, Adv. Funct. Mater., 2020, 30, 1907951.
- 36 L.-H. Zeng, D. Wu, S.-H. Lin, C. Xie, H.-Y. Yuan, W. Lu, S. P. Lau, Y. Chai, L.-B. Luo, Z.-J. Li and Y. H. Tsang, Adv. Funct. Mater., 2019, 29, 1806878.
- 37 J.-M. Liu, Photonic devices, Cambridge University Press, 2009.
- 38 L. Wang, J.-J. Li, Q. Fan, Z.-F. Huang, Y.-C. Lu, C. Xie, C.-Y. Wu and L.-B. Luo, J. Mater. Chem. C, 2019, 7, 5019-5027.
- 39 K. Zhou, J. Shen, X. Li, X. Hong, W. Feng, X. Tang, X. Jiang, D. Wei, Y. Chen, X. Liu, Y. Xie, D. Wei and T. Sun, Phys. E, 2020, 123, 114147.
- 40 C. Yim, N. McEvoy, S. Riazimehr, D. S. Schneider, F. Gity, S. Monaghan, P. K. Hurley, M. C. Lemme and G. S. Duesberg, Nano Lett., 2018, 18, 1794-1800.
- 41 D. Wu, C. Jia, F. Shi, L. Zeng, P. Lin, L. Dong, Z. Shi, Y. Tian, X. Li and J. Jie, J. Mater. Chem. A, 2020, 8, 3632-3642.
- 42 L.-H. Zeng, S.-H. Lin, Z.-J. Li, Z.-X. Zhang, T.-F. Zhang, C. Xie, C.-H. Mak, Y. Chai, S. P. Lau, L.-B. Luo and Y. H. Tsang, Adv. Funct. Mater., 2018, 28, 1705970.
- 43 D. Wu, Y. Wang, L. Zeng, C. Jia, E. Wu, T. Xu, Z. Shi, Y. Tian, X. Li and Y. H. Tsang, ACS Photonics, 2018, 5, 3820-3827.
- 44 H. Qiao, Z. Huang, X. Ren, S. Liu, Y. Zhang, X. Qi and H. Zhang, Adv. Opt. Mater., 2020, 8, 1900765.
- 45 Q. Liang, Q. Wang, Q. Zhang, J. Wei, S. X. Lim, R. Zhu, J. Hu, W. Wei, C. Lee, C. Sow, W. Zhang and A. T. S. Wee, Adv. Mater., 2019, 31, 1807609.
- 46 S. Hao, J. Zeng, T. Xu, X. Cong, C. Wang, C. Wu, Y. Wang, X. Liu, T. Cao, G. Su, L. Jia, Z. Wu, Q. Lin, L. Zhang, S. Yan,

- M. Guo, Z. Wang, P. Tan, L. Sun, Z. Ni, S.-J. Liang, X. Cui and F. Miao, Adv. Funct. Mater., 2018, 28, 1803746.
- 47 W. Yu, S. Li, Y. Zhang, W. Ma, T. Sun, J. Yuan, K. Fu and O. Bao, Small, 2017, 13, 1700268.
- 48 L. Ye, H. Li, Z. Chen and J. Xu, ACS Photonics, 2016, 3, 692-699.
- 49 R. K. Ulaganathan, Y.-Y. Lu, C.-J. Kuo, S. R. Tamalampudi, R. Sankar, K. M. Boopathi, A. Anand, K. Yadav, R. J. Mathew, C.-R. Liu, F. C. Chou and Y.-T. Chen, Nanoscale, 2016, 8, 2284-2292.
- 50 X. Zhou, L. Gan, W. Tian, Q. Zhang, S. Jin, H. Li, Y. Bando, D. Golberg and T. Zhai, Adv. Mater., 2015, 27, 8035-8041.
- 51 G. W. Mudd, S. A. Svatek, L. Hague, O. Makarovsky, Z. R. Kudrynskyi, C. J. Mellor, P. H. Beton, L. Eaves, K. S. Novoselov, Z. D. Kovalyuk, E. E. Vdovin, A. J. Marsden, N. R. Wilson and A. Patanè, Adv. Mater., 2015, 27, 3760-3766.
- 52 X. Wang, P. Wang, J. Wang, W. Hu, X. Zhou, N. Guo, H. Huang, S. Sun, H. Shen, T. Lin, M. Tang, L. Liao, A. Jiang, J. Sun, X. Meng, X. Chen, W. Lu and J. Chu, Adv. Mater., 2015, 27, 6575-6581.
- 53 G. Su, V. G. Hadjiev, P. E. Loya, J. Zhang, S. Lei, S. Maharjan, P. Dong, P. M. Ajayan, J. Lou and H. Peng, Nano Lett., 2015, 15, 506-513.
- 54 J. Mao, Y. Yu, L. Wang, X. Zhang, Y. Wang, Z. Shao and J. Jie, Adv. Sci., 2016, 3, 1600018.
- 55 R. Zhuo, L. Zeng, H. Yuan, D. Wu, Y. Wang, Z. Shi, T. Xu, Y. Tian, X. Li and Y. H. Tsang, Nano Res., 2019, 12, 183-189.
- 56 F. Wang, Z. Wang, K. Xu, F. Wang, Q. Wang, Y. Huang, L. Yin and J. He, Nano Lett., 2015, 15, 7558-7566.
- 57 S. R. Tamalampudi, Y.-Y. Lu, U. Rajesh Kumar, R. Sankar, C.-D. Liao, B. Karukanara Moorthy, C.-H. Cheng, F. C. Chou and Y.-T. Chen, Nano Lett., 2014, 14, 2800-2806.
- 58 M. Sajjad, N. Singh, M. De Bastiani, S. De Wolf and U. Schwingenschlögl, Phys. Status Solidi RRL, 2019, 13, 1900328.
- 59 K. K. N. Simon and M. Sze, Physics of Semiconductor Devices, Wiley, New Jersey, 2006.
- 60 A. P. S. Gaur, S. Sahoo, M. Ahmadi, S. P. Dash, M. J. F. Guinel and R. S. Katiyar, Nano Lett., 2014, 14, 4314-4321.
- 61 P. K. Chow, E. Singh, B. C. Viana, J. Gao, J. Luo, J. Li, Z. Lin, A. L. Elías, Y. Shi, Z. Wang, M. Terrones and N. Koratkar, ACS Nano, 2015, 9, 3023-3031.
- 62 M. Alves, A. Pérez-Rodríguez, P. J. Dale, C. Domínguez and S. Sadewasser, J. Phys.: Energy, 2019, 2, 012001.
- 63 X. Li, Y. Jung, K. Sakimoto, T.-H. Goh, M. A. Reed and A. D. Taylor, Energy Environ. Sci., 2013, 6, 879-887.